High-energy diffraction dissociation of K_L^0 into exclusive final states

M. J. Lamm,[a] J. E. Wiss, P. Avery,[b] J. Butler,[a] G. Gladding, M. C. Goodman,[c]
T. O'Halloran, J. J. Russell,[d] A. Wattenberg, J. Busenitz,[e] P. Callahan,[f] and C. Olszewski[f]
University of Illinois, Urbana, Illinois 61801

M. Binkley, J. P. Cumalat,[g] I. Gaines, M. Gormley, J. Peoples, and D. Harding
Fermi National Accelerator Laboratory, Batavia, Illinois 60510

M. S. Atiya,[h] E. P. Hartouni,[i] S. D. Holmes,[a] B. C. Knapp, W. Lee, R. Seto, and
W. Wisniewski[j]
Columbia University, New York, New York 10027

(Received 17 April 1987; revised manuscript received 7 August 1987)

We have observed diffraction dissociation of K_L^0 mesons with a carbon target into the exclusive final states $K_S^0\pi^+\pi^-$, $K_S^0\omega$, and $K_S^0\phi$. The diffraction production cross section for these states is not strongly dependent on the incident energy, varying at most by 30% between 75 and 150 GeV. The mass distributions do not change appreciably as a function of laboratory energy. The ratio of the diffractive mass-threshold production of $K^{*\pm}\pi^{\mp}$, $K_S^0\rho$, $K_S^0\omega$, and $K_S^0\phi$ is compared with previously obtained lower-energy data.

I. INTRODUCTION

We present results on the diffraction dissociation of K_L^0 in K_L^0-carbon collisions into the $K_S^0\pi^+\pi^-$, $K_S^0\omega$, and $K_S^0\phi$ exclusive final states over an incident K_L^0 energy range from 75 to 200 GeV (Ref. 1). Data are presented on the forward $|t-t_{\min}|$ dependence in the diffractive peak, the energy dependence of the three exclusive cross sections, and the mass distribution of the diffractive system. Each of these final states shows an exponentially falling $|t-t_{\min}|$ distribution with a slope consistent with that expected for the coherent scattering from the carbon nucleus. The cross sections for the three exclusive final states are observed to be nearly energy independent over the range of energies explored in this experiment. The mass distributions of the $K_S^0\omega$ and $K_S^0\phi$ final states are essentially structureless and fall sharply from threshold in a way which is nearly independent of incident beam energy. The mass distribution of the $K_S^0\pi^+\pi^-$ final state shows structure in the Q region[2-5] near 1.3 GeV but no strong evidence for structure in the L region[2,3] near 1.8 GeV. A further analysis of the $K_S^0\pi^+\pi^-$ final state shows large contributions from the $K^{*\pm}\pi^{\mp}$ and $K_S^0\rho$ final states. Finally, we compare the cross sections for K_L^0 diffraction dissociation into the quasi-two-body states $K_S^0\phi$, $K_S^0\omega$, $K^{*\pm}\pi^{\mp}$, and $K_S^0\rho$.

II. THE EXPERIMENT

The data reported in this paper came from two experiments which were conducted in the broadband neutral beam at Fermilab located in the east area of the proton lab. The first of these experiments, E87, studied the photoproduction of multibody final states with an emphasis on charmed-particle photoproduction. The second of these experiments, E401, studied the photoproduction of low-multiplicity final states with an emphasis on vector-meson photoproduction. The K_L^0 diffraction-dissociation results presented in this paper derive from the E87 data. The E401 data played a crucial role in establishing the shape and normalization of the K_L^0 component of the neutral beam since it had a far less severe triggering bias.

A. The neutral beam

Both experiments employed a zero degree neutral secondary beam created by impinging primary protons on a 40-cm beryllium primary target located approximately 180 m upstream of the experiment's secondary target. The primary proton beam had an energy of 400 GeV in E87 and an energy of 350 GeV in E401. The beam then passed through 34 m of liquid deuterium designed to preferentially absorb neutral hadron contamination (primarily neutrons and K_L^0's) relative to the photons (produced primarily from π^0 and η^0 decays). After passing through the deuterium the resultant beam consisted nearly entirely of photons with a few percent contribution of K_L^0's and neutrons (a quantitative analysis is presented in Sec. III). Although the deuterium filtering system produced an acceptably clean photon beam for E401 and E87, the number of K_L^0 induced events collected in these experiments was comparable to the yield of photoproduced events owing to the much larger K_L^0 total cross section.

B. Running conditions

In order to monitor the large fraction of K_L^0 and neutron-initiated events, E87 took data under two alternating beam conditions. In the "photon" running, the deuterium filtered neutral beam impinged directly on the

experiment's target. In the "lead" running, six radiation lengths of lead, inserted in a collimated sweeping magnet, eliminated essentially all high-energy photons prior to the beam striking the experiment's target. Approximately 43% of the E87 luminosity was taken under the "lead" running conditions with the goal of providing a method for estimating the nonphoton background to photoproduced final states. Within the context of this paper, the lead running condition provides an essentially photon free beam, dominated by K_L^0's except at energies beyond 150 GeV where neutron contamination becomes substantial.

C. Apparatus

A complete description of the E87 apparatus has been published in Ref. 6. We will summarize aspects of the E87 apparatus with an emphasis on those details particularly relevant to the results presented in this paper. E87 employed an active target which was comprised of 20 segments of scintillator with dimensions of 75 mm$\times$75 mm$\times$1 mm. Each scintillator was individually wrapped in 75-μm-thick aluminum foil in order to optically isolate it from adjacent scintillators. The resultant target assembly represented 3% of an interaction length, or 4% of a radiation length and consisted of 91% carbon, 8% hydrogen, and 1% aluminum by weight. Two photomultipliers measured the light yield of each scintillator segment. The photomultiplier signals were combined and sent to one analog-to-digital converter (ADC) per scintillator. The discriminated signals from the last two segments of the target assembly form part of the experimental trigger and established the basic timing strobe of the experiment. We shall refer to the E87 target assembly as the τ target in recognition of its anticipated (but unrealized) role in tagging photoproduced charmed particles through their finite lifetime.

A multiparticle magnetic spectrometer enhanced with significant particle-identification capabilities analyzed the final-state particles which emerged from interactions in the τ target (see Fig. 1). The magnetic spectrometer consisted of two vertically bending magnets interspersed with five stations of multiwire proportional chambers (MWPC's). Each MWPC station consisted of three

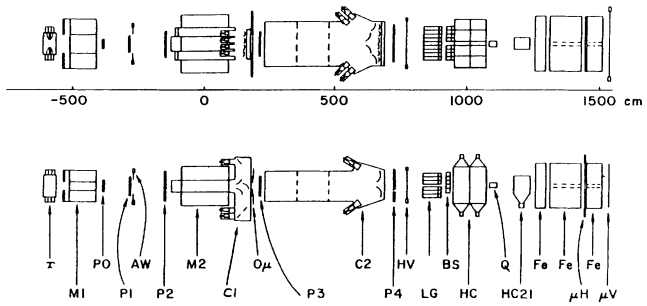

FIG. 1. A plan view (top) and elevation view (bottom) of the E87 detector. In E401 the active scintillation target counter (τ) was replaced with a liquid-hydrogen target and a downstream target counter.

planes of sense wires orientated to provide coordinate information in the horizontal direction and at $\pm 11.3°$ with respect to the vertical direction. The first analysis magnet (called $M1$ in Fig. 1) was positioned immediately downstream of the τ target and was followed by three proportional-chamber stations called $P0$, $P1$, and $P2$. The second analysis magnet ($M2$) followed $P2$ and was followed by the remaining two chamber stations $P3$ and $P4$. The two analysis magnets ran with opposite polarity and had momentum kicks of 0.40 and 0.62 GeV, respectively. The momentum of a particle which traversed all five chamber stations was measured from the difference between the vertical angle measured upstream of $M2$ (in $P0$–$P2$) and the vertical angle downstream of $M2$ (in $P3$ and $P4$). The momentum of a wide-angle (or low-momentum) particle which traversed the first three chamber stations but failed to traverse the aperture of $M2$ was computed by extrapolating the track segment measured from $P0$–$P2$ back to either the primary event vertex or a secondary vertex in the case of a K_S^0 decay.

The MWPC wire spacing was 1 mm in the planes of $P0$ and 2 mm in all remaining planes except in the nonbend view of $P4$ where the wire spacing was 3 mm. The position resolution of this system was improved in $P1$–$P4$ by recording drift-time information in a set of time-to-digital converters (TDC's) called time-recorder modules (or TRM's). Each of the planes in chambers $P1$–$P4$ was divided into 32 contiguous sections called TRM bands with the number of wires per band contoured to the anticipated multiplicity. The summed output from a given TRM band was compared to the timing signal from the τ target to provide drift time information. In addition, the TRM information provided information of the event multiplicity and topology for triggering purposes.

A 90-element lead-glass array located downstream of $P4$ provided photon detection and electron identification. A fine section consisting of 6.35 cm$\times$6.35 cm blocks (transverse to the beam direction) was surrounded by a coarser section of 15.25 cm$\times$15.25 cm blocks. The blocks were approximately 20 radiation lengths thick along the beam direction. A photomultiplier tube was attached directly to the end of each lead-glass block for read out. Since all bending in the E87 spectrometer was done vertically, Bethe-Heitler pairs were very intense in the median vertical plane. In order to retard radiation damage to the lead glass, two separate stacks were constructed which were separated by a 10.2-cm vertical gap. The array was calibrated using e^+e^- pairs and monitored for stability using a neon discharge lamp. The 90 elements were run with approximately equal gain to allow for their use in a total-energy trigger condition.

Two multicell Cherenkov counters provided charged-particle identification. The lower threshold counter, called $C1$ in Fig. 1, was positioned in the aperture of $M1$ and had 12 cells. $C1$ contained atmospheric nitrogen gas and thus had a pion threshold of 5.85 GeV. An average of 12 photoelectrons were generated for a $\beta=1$ particle traversing the $C1$ radiator volume. $C2$ was located between $P3$ and $P4$ and had 16 cells. $C2$ contained an atmospheric helium-nitrogen mixture which

gave it a pion threshold of 10.7 GeV and an average of six photoelectrons for a $\beta=1$ particle. Such a system provided unambiguous kaon identification in the range from 22–40 GeV for particles with unconfused Cherenkov patterns in both $C1$ and $C2$. Kaons could be separated from pions over the extended energy range from 6–40 GeV.

Hodoscopes of horizontally (μH) and vertically (μV) orientated scintillation counters shielded by large steel blocks provided muon for tracks traversing the aperture of $M2$.

D. Triggers

We turn next to a discussion of those portions of the apparatus which are primarily used in the experimental trigger. This trigger served to greatly reduce the contribution of Bethe-Heitler pairs relative to the far less copious multihadronic events which were of interest to the experimenters. The trigger was accomplished in two stages—a fast master-gate decision and a slower logical decision called the DC logic.

The master gate was derived from signals from the τ target and a scintillation hodoscope called the $H\times V$ array. The $H\times V$ array consisted of a set of vertically and horizontally orientated scintillation counters located directly downstream of $P4$. The response of the $H\times V$ array was fed into a logic unit which counted the number of coincidences between a given H counter and a matching V counter. The master gate required two such $H\times V$ coincidences and required signals from the two most downstream elements of the τ target. The $H\times V$ array was made in two vertical halves which were separated by a central 10.2-cm gap. The $H\times V$ requirement suppressed the Bethe-Heitler pairs which tightly populate the vertical median plane because of the orientation of the two bending magnets. A successful master gate created a 250-nsec dead time which allowed the DC logic sufficient time to make a decision.

The DC logic used information from additional scintillation counters, multiplicity and event topology information from the MWPC system, and energy-deposition information both from the lead-glass array and a hadronic calorimeter located downstream of the lead-glass array. The additional scintillation counters used in the trigger included four scintillation counters (AW) which formed a frame immediately outside the fiducial volume of $P1$ and could be used to reject events with additional wide-angle tracks outside the acceptance of the MWPC system. Two other scintillation-counter systems were used to reject events which were not initiated by neutral incident particles from the neutral beamline. The central region was covered by a 30-cm-wide vacuum counter (A_0) which was designed to veto charged particles traveling along the beam line. The outer section consisted of a hodoscope of counters (A_μ) which vetoed events initiated by or accompanying a muon from the muon halo.

Trigger information from the MWPC system was derived from the fast signals generated by the TRM electronics. The median number of hits in the three planes which comprised a chamber station served to measure the charged track multiplicity striking a given chamber. Additional information on the event topology was obtained by dividing the TRM information for planes which measure the nonbend view into three regions—central, inner, and outer. The central region comprised the central six centimeters which was dominated by Bethe-Heitler pairs, the inner region comprised the bulk of the chamber fiducial volume, and the outer region used the four outermost TRM bands of $P1-P4$.

The DC-logic decision was organized on two levels in order to provide flexibility. The response of individual detectors served to set a maximum of 16 possible bus lines. These bus lines were bused to a set of pin-logic modules. Each experimental trigger was derived from the response of a separate pin logic module which fired based on the presence or absence of selected bus lines. Each pin-logic module had an associated prescale module which would allow the signal from the pin-logic module to create an event trigger an adjustable fraction of the time. The use of prescaled triggers allowed for the simultaneous collection of events under both relatively unbiased and heavily biased triggering conditions.

The data presented here were collected under triggering conditions which we call the hadron trigger. This trigger required a trigger multiplicity between three and ten tracks, with at least two tracks in the inner TRM region, and required that neither the A_0, AW, nor A_μ array was set. The hadron trigger also required that the sum of lead-glass and hadronic-calorimeter energy be in excess of 75 GeV with at least 42 GeV deposited in the hadron calorimeter.

III. THE K_L^0 SPECTRUM

In this section we describe measurements of the K_L^0 spectrum determined through observation of K_L^0 decaying into the $\pi^+\pi^-\pi^0$, $\pi\mu\nu$, and $\pi e\nu$ final states. The E87 trigger was heavily biased against these decay modes. For this reason the K_L^0 spectrum was measured using data collected under the far less biased trigger present in E401. The resultant spectrum shape was found to be in substantial agreement to the inclusive K_S^0 spectrum reported by Edwards *et al.*[7] The Edwards *et al.*, parametrization provided a method for extrapolating the E401 data which were taken with a primary proton beam energy of 350 GeV up to 400 GeV, the primary-proton-beam energy used in E87.

E401 offered several major advantages in determining the K_L^0 spectrum by measuring events which consisted of the products of a single K_L^0 decay. The measurement of the diffractive vector-meson photoproduction cross section was a major goal of E401. Many of the features of low-mass vector-meson decays (such as $\phi\rightarrow K^+K^-$) strongly resembles the decays of the K_L^0 in that events have low final-state multiplicities and at high energies the decay products are produced at small angles with respect to the beam axis. In order to accommodate such topologies, the E401 trigger required fewer final-state tracks and the gap between the $H\times V$ counters was reduced compared to the gap in E87. Finally, the total en-

ergy requirement in E401 was reduced to 50 GeV in contrast with the 75 GeV required in E87.

For a variety of reasons we found that the $K_L \to \pi\mu\nu$ decay mode was the most suitable signal to use for establishing the K_L^0 energy spectrum. Because this decay mode includes an undetectable neutrino, its signature is less direct than the signature for the fully reconstructed decay mode $K_L \to \pi^+\pi^-\pi^0$. For this reason we take some care in establishing the legitimacy of the $\pi\mu\nu$ signal demonstrating that it is relatively free of background.

Figure 2(A) shows the $\pi^+\pi^-$ mass ($M_{\pi\pi}$) distributions for two track events with cuts on $P_\perp$ balance and track unassociated shower energy chosen to assure exclusivity. The $M_{\pi\pi}$ spectrum is dominated by the $\rho(770)$ produced by the photon contribution of the E401 neutral beam. The vertex Z distribution for these ρ events, shown in Fig. 2(B), shows enhancements in the area of the E401 H_2 cryogenic target and T_0 trigger counter.

Figure 3(A) shows the $M_{\pi^+\pi^-\pi^0}$ plot for events with balanced $P_\perp$ consisting of two tracks and two showers (not associated with tracks) in the lead-glass array. A relatively narrow mass peak is observed at the mass of the K_L^0 along with a mass peak signifying photoproduced $\omega \to \pi^+\pi^-\pi^0$ events. The Z vertex distribution for events within the K_L^0 mass peak is shown in Fig. 3(b). The distribution of Fig. 3(B) is essentially flat over the region from the location of the A_0 veto and T_0 and shows no evidence of an enhancement in the Z regions filled with matter. One expects a uniform Z distribution

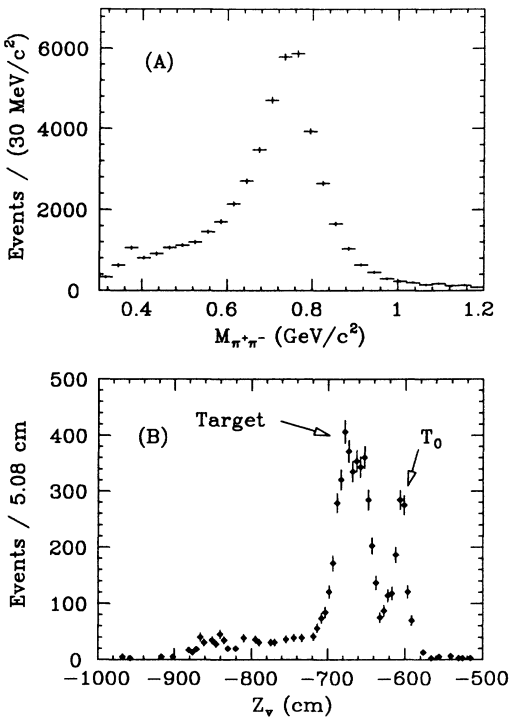

FIG. 2. E401 diffractive $\pi^+\pi^-$ events: (A) $M_{\pi^+\pi^-}$ and (B) Z vertex distributions.

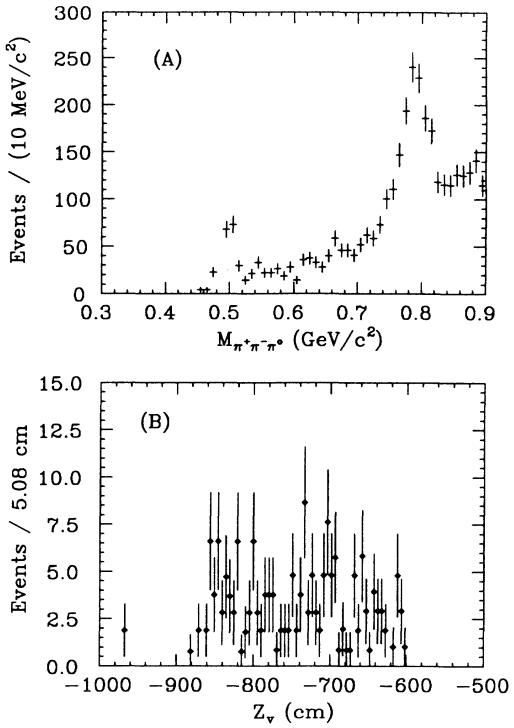

FIG. 3. E401 $\pi^+\pi^-\pi^0$ $P_\perp$-balanced events: (A) $M_{\pi^+\pi^-\pi^0}$ and (B) Z vertex distributions.

for events which represent the decay of K_L^0's rather than events due to the interaction of the beam in target material.

Figure 4(A) shows the $M_{\pi\pi}$ spectrum for events with one track identified as an electron using information from the lead-glass array. A clear mass peak in Fig. 4(A) at the $\rho(770)$ is observed which corresponds to incorrectly identified, photoproduced $\rho \to \pi^+\pi^-$ decays. The solid line superimposed over the data represents the Monte Carlo prediction (described below) from a $K_L \to \pi e\nu$ kinematic reflection. The area of the curve is normalized to the area associated with the lower-mass peak. The region with $M_{\pi\pi} < 0.570$ GeV/c^2 has the shape expected for $K_L \to \pi e\nu$ decay. The Z vertex distribution for events in the K_L^0 mass region (below 0.5 GeV/c^2), shown in Fig. 4(b), is consistent with being flat between the A_0 and T_0 triggering counters as expected for K_L^0 candidates.

Figure 5(a) shows the $M_{\pi\pi}$ distributions for two track events with one track positively identified as a muon by the muon counters. A far less prominent ρ peak (relative to the K_L^0 region) is observed in Fig. 5(b) compared to the peak seen in $e\pi$ events thus indicating that muons are relatively uncontaminated by pions. The solid line superimposed over the data represents the Monte Carlo prediction from a $K_L \to \pi\mu\nu$ kinematic reflection with the curve normalized to the area associated with the lower-mass peak. Again, there is good agreement between the data and Monte Carlo prediction. The Z vertex distribution for the events in the $M_{\pi\pi} < 0.500$ GeV/c^2 region, shown in Fig. 5(b), is consistent with be-

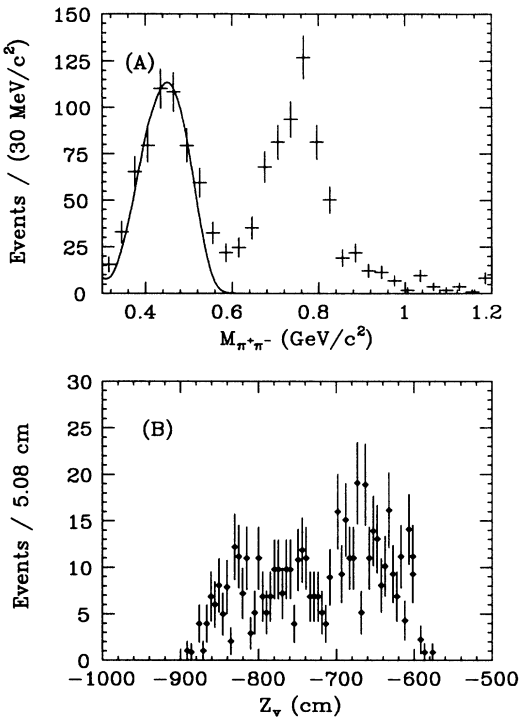

FIG. 4. E401 two-track events with one track identified as an electron: (A) $M_{\pi^+\pi^-}$ distribution with Monte Carlo prediction of kinematic reflection from $K_L \to \pi e \nu$ superimposed and (B) Z vertex distribution.

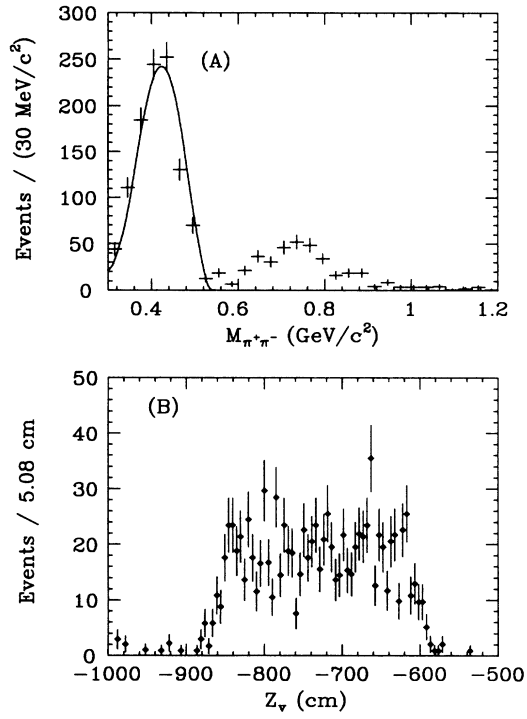

FIG. 5. E401 two-track events with one track identified as a muon: (A) $M_{\pi^+\pi^-}$ distribution with Monte Carlo prediction of kinematic reflection from $K_L \to \pi\mu\nu$ superimposed and (B) Z vertex distribution.

ing uniform throughout the K_L^0 decay volume.

In addition to providing the largest sample size, the $K_L \to \pi\mu\nu$ decay sample has a wider range of momentum with reasonable reconstruction efficiency than either of the other two decay modes which we have discussed. Isolation of the K_L^0 candidates in either the $\pi^+\pi^-\pi^0$ or πe decay mode requires information from the lead-glass array which introduces a severe K_L^0 momentum bias owing to the central gap of this device. This gap was necessary owing to the copious flux of Bethe-Heitler pairs in the central region which would cause radiation damage to any lead glass. At high momenta, the γ's from π^0 decay or the electrons from the $\pi e \nu$ decay mode tend to populate the region in or near to the gap thus destroying the lead-glass information. For these reasons the K_L^0 energy spectrum was measured entirely from the $\pi\mu\nu$ decay candidates.

We have compared the energy spectrum deduced from our $K_L^0 \to \pi\mu\nu$ candidates to a Monte Carlo calculation based on data of Edwards *et al.* who measured the production of K_S^0 at zero degrees from a beryllium target.[7] Edwards *et al.* found the empirical relationship

$$E\frac{d^3\sigma}{dp^3} = R(1-X)^F[1+D(1-X)^4] ,$$

where

$$R = 5.6 \pm 0.8 \text{ mb/GeV}^2, \quad F = 3.4 \pm 0.2 ,$$

$$D = 0.8 \pm 0.7, \quad X = E_{K_L}/E_{\text{beam}} .$$

We have written a Monte Carlo program to simulate the $K_L^0 \to \pi\mu\nu$ candidates observed in E401 data. The K_L^0's were generated according to the parametrization of Edwards *et al.*, traced through the geometry and apertures of the neutral beam line, and were attenuated due to both K_L^0 decay and hadronic absorption within the liquid-deuterium filter. The $K_L^0 \to \pi\mu\nu$ decay process was simulated for events which decayed in the E401 triggerable decay volume using the matrix element provided by Greenhalgh.[8] This matrix element caused only minor deviations from phase-space K_L^0 decay.

An estimate for the energy of a K_L^0 in $K_L^0 \to \pi\mu\nu$ events can be determined from the four-vectors of the $\pi\mu$ system by demanding $P_\perp$ balance and by constraining the mass of the $\pi\mu\nu$ system to the K_L^0 mass. Because there is a twofold ambiguity to the resulting energy of the ν depending on whether the neutrino is produced in the forward or backward hemisphere in the K_L^0 rest frame, we use the average of the two solutions as an estimate of the K_L^0 energy. Typically, this K_L^0 energy estimate had an uncertainty (σ) of 20 GeV. Figure 6 compares the measured K_L^0 spectrum in the E401 data to the Monte Carlo calculation. The Monte Carlo calculation incorporated resolution effects on the K_L^0 energy estimator because of a measurement error on the $\pi\mu$ momenta as well as the twofold ambiguity as to the neutrino direction. We note that the Monte Carlo yield was absolutely normalized to the cross section of Edwards *et al.* Hence the spectrum of E401 $K_L^0 \to \pi\mu\nu$ events are consistent with previous measurements in both shape and absolute

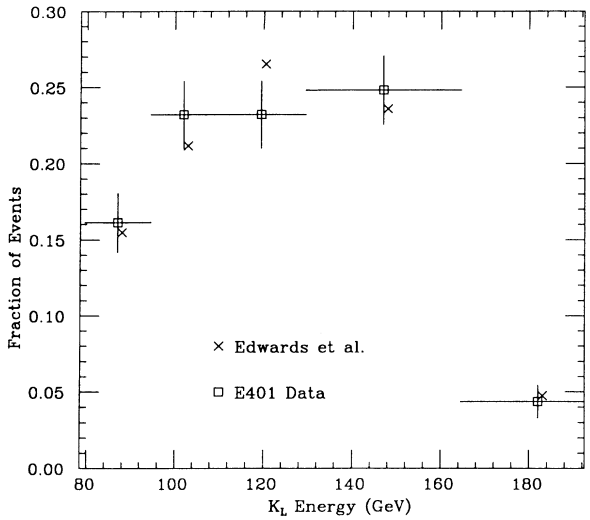

FIG. 6. Comparison of E401 measured K_L^0 spectrum with the parametrization of Edwards *et al.*

normalization. The absolute normalization of the Monte Carlo calculation implied that there were $(0.42\pm0.040)\times10^{-8}$ K_L^0's in the energy range from 75 to 200 GeV per incident proton delivered to the E401 primary target.

Several assumptions were used to deduce the shape and normalization of the E87 K_L^0 energy spectrum which was run at a slightly higher primary proton energy (400 GeV compared to 350 GeV) and with different beam line collimators than used in E401. The parametrization of Edwards *et al.*, uses a scaling variable X which allows one to extrapolate yields to the slightly higher incident proton energy. In order to correct for the difference in beam line collimators, we assumed that the ratio of K_L^0's to photons in the energy range from 75 to 200 GeV was the same in E401 and E87. Both experiments measured the photon spectral shape by explicit reconstruction of Bethe-Heitler pairs and normalized this spectrum using the total beam power measured by a Wilson quantameter. The K_L^0 normalization for the lead running of E87 was obtained by assuming that the K_L^0 to primary proton ratio in lead running was the ratio obtained in photon running with a slight correction due to additional K_L^0 absorption in the $\approx20\%$ of an interaction length of lead inserted into the beam.

IV. ANALYSIS

A. Overview

During E87 approximately 3×10^7 events were recorded on 1200 800-BPI magnetic tapes. In the first stage of the analysis charged tracks were reconstructed using the 15-plane MWPC system. Tracks were classified into two types: tracks that traversed the entire spectrometer and tracks that left the detector before the downstream magnet and Cherenkov counters. In the next stage the reconstructed tracks were used to define a target vertex and to form K_S^0 and Λ^0 candidates. The Cherenkov counter information was then matched to the track vectors to distinguish π's from kaons from protons in limited momentum regions. Throughout this analysis the Cherenkov information was only used in distinguishing K_S^0's from Λ^0's. The lead-glass pulse heights were converted to energy-shower depositions and shower cluster patterns were found. Finally, data summary tapes were produced from these reconstructed events for topologies of interest.

B. Reconstruction of K_S^0

K_S^0 reconstruction in our spectrometer involves matching two oppositely charged tracks which appear to form a vertex downstream of the primary event vertex. Ambiguities arise when one or both of the tracks appear to point back to the target. In order to obtain a clean sample, we require that at least one track traverse the two magnet/two Cherenkov system and that at least one track not be associated with the primary vertex. The $\pi^+\pi^-$ mass spectrum is shown in Fig. 7. by restricting the $\pi^+\pi^-$ mass combinations to be within 15 MeV/c^2 of the K_S^0 mass, we obtain a K_S^0 sample which has a background of approximately 10%.

C. π^0 reconstruction

We associate adjacent blocks of energy depositions in the lead-glass array as showers from photons or hadrons. The position of each shower is determined from the amount of energy sharing between the most energetic block and the adjacent associated ones, using an empirical formula derived in Ref. 9.

A major difficulty in π^0 reconstruction is the misidentification of showers produced by hadrons with showers produced by photons. We studied the pattern of hadron shower deposition in our lead-glass array by using elastic photoproduced ρ's from E401. We extrapolate the position of the π from a ρ decay to the lead-

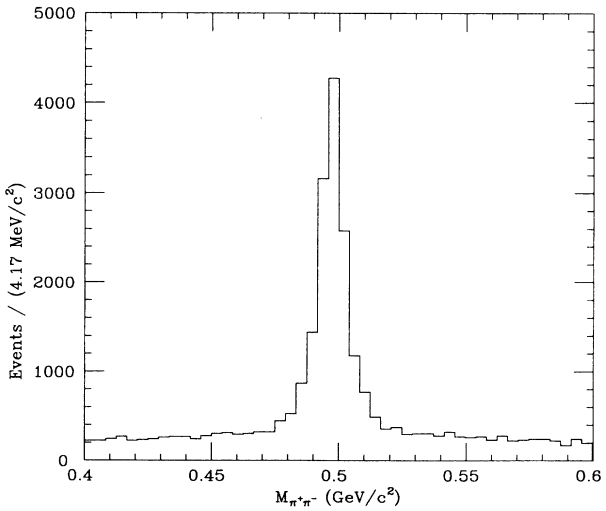

FIG. 7. $\pi^+\pi^-$ mass distribution for K_S^0 candidates.

glass array and measure the transverse distance from this point to the center of the lead-glass shower clusters. Showers whose centers were within a certain radius of the track position would be considered associated with the charged track and hence would not be included in the photon sample. This "track to shower radius" is parametrized as a function of shower energy and lead-glass block size. The radius is chosen such that, on average, 95% of the pion energy in the lead glass will be deposited in showers whose centers are in this radius.

Figure 8 shows the γ-γ invariant-mass distribution for the two most energetic showers not associated with a charged hadron in an event. A clear π^0 is seen with a full width at half maximum (FWHM) of 40 MeV/c^2. For the purpose of reconstructing $\omega \to \pi^+\pi^-\pi^0$, a π^0 is defined as two photons with an invariant mass within 20 MeV/c^2 of the π^0 mass.

D. Data set/diffractive cuts

The data set under investigation consists of four final-state tracks: two from a good K_S^0 plus two oppositely charged tracks assigned to the primary-event vertex. In addition, the four largest energy depositions unassociated with a charged track are used to form π^0's.

To help ensure exclusivity, we demand that (1) the wide-angle veto counters (AW) be off, (2) there are only four charged tracks per event, and (3) the amount of neutral energy not associated with a charged track or a photon be less than 10 GeV. The 10-GeV cut is motivated by the study of photoproduced elastic ρ's as mentioned above. Because the $|t-t_{\min}|$ distribution measures the contribution from coherent and non-coherent production, we demand that (4) the measured $|t-t_{\min}|$ of a final state be less than 0.05 GeV^2, which is well within the coherent forward peak. These four cuts constitute the "diffractive" cuts on the data.

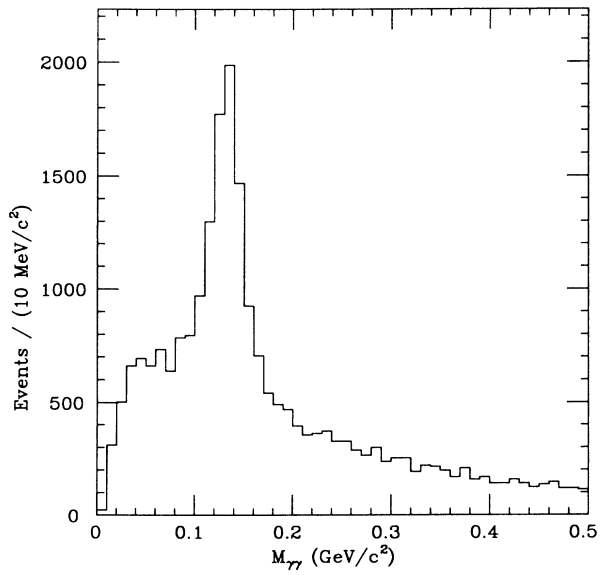

FIG. 8. $\gamma\gamma$ mass distribution in $K_S^0\pi^+\pi^-$ events using the two most energetic shower clusters in the lead glass which were not associated with a charged track.

E. Determining acceptances

Each event is weighted by a detection efficiency which is a function of the system's laboratory energy, mass, and center-of-mass angular distribution. We accomplish this by computing the detection efficiency for Monte Carlo events with discrete values for mass, laboratory energy, and Dalitz-plot location. We integrate over those parameters whose distributions are known (such as the lifetime of the K_S^0) or do not appreciably effect the acceptance (such as the $|t-t_{\min}|$ distribution and angular distributions). We have assumed that the center-of-mass angular distribution for three-body decays is isotropic. The acceptance for each data point is then computed from an interpolation between the discrete Monte Carlo points.

In an effort to eliminate some of the systematic errors associated with computing detection efficiencies, the generated Monte Carlo event four-vectors are used to produce a data tape in the raw event form. Hence the Monte Carlo and real data are analyzed by the same reconstruction programs.

Hadronic shower deposition in the lead glass, and its effect on π^0 reconstruction is handled separately, because of the complexity of generating hadronic showers in our lead-glass detector. We again use elastic photoproduced ρ's from experiment 401 with Monte Carlo–generated photons, to study the photon confusion probability as a function of photon energy, track-shower center radius, and lead-glass block size. We compute the detection efficiency for a photon from an $\omega \to \pi^+\pi^-\pi^0$ if its lead-glass shower is outside of this track to shower-center radius.

V. RESULTS

The similarities among the final states $K_S^0\pi^+\pi^-$ ($K_S^0\rho$, $K^{*\pm}\pi^{\mp}$), $K_S^0\omega$, and $K_S^0\phi$ are demonstrated by comparing their kinematic distributions $|t-t_{\min}|$, mass distribution as a function of E_{lab}, and cross section as a function of $\sqrt{s}$. For the $K_S^0\omega$ and $K_S^0\phi$ energy and mass distributions, we use both the photon and lead data in order to increase our event statistics. Since the particle identification of the K_S^0, ω, and ϕ will be shown to be unambiguous, the background from photon as well as neutron-produced final states is small. For the $K_S^0\pi^+\pi^-$ study, we use only lead data to eliminate the background of diffractively photoproduced $K_S^0K^{\pm}\pi^{\mp}$ final states.

A. $|t-t_{\min}|$

We compare the $|t-t_{\min}|$ distribution for $K_S^0\pi^+\pi^-$, $K_S^0\omega$, and $K_S^0\phi$ events. Figure 9(A) shows the $|t-t_{\min}|$ distribution for all $K_S^0\pi^+\pi^-$ that satisfy diffractive cut criteria 1–3, while Fig. 9(B) shows the same distribution for those events that fail the 10-GeV unassociated lead-glass energy cut. No coherent peak is observed in the excess lead-glass energy data.

Using the three diffractive cuts we plot the $\pi^+\pi^-\pi^0$

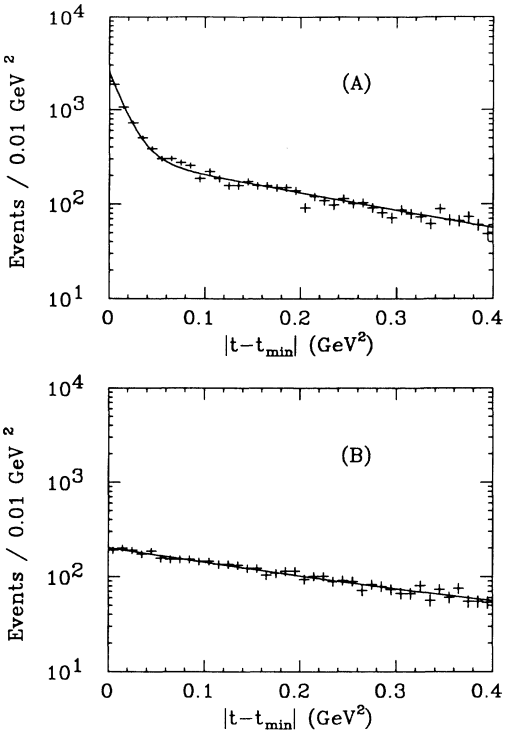

FIG. 9. $|t-t_{min}|$ distribution for $K_S^0\pi^+\pi^-$ events satisfying diffractive cuts 1–3 (see text): (A) <10 GeV neutral energy and (B) >10 GeV neutral energy. The solid lines represent a fit of the distributions to the sum of two exponentials.

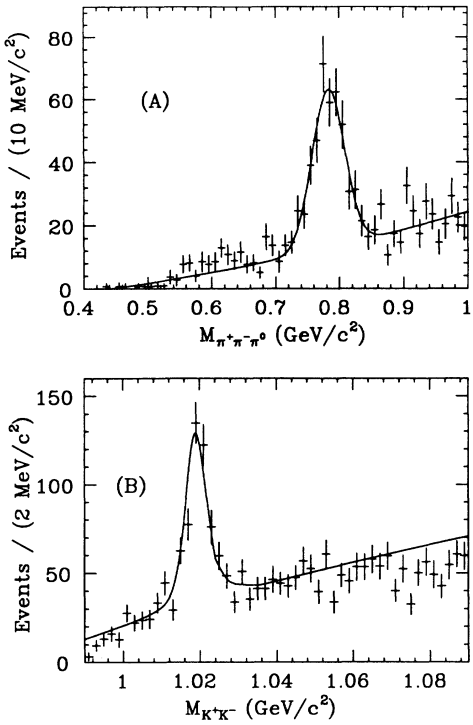

FIG. 10. Subresonance mass plot: (A) $\pi^+\pi^-\pi^0$ in $K_S^0\pi^+\pi^-\pi^0$ events and (B) K^+K^- in $K_S^0K^+K^-$ events.

invariant mass for $K_S^0\pi^+\pi^-\pi^0$ events. Since our ω mass resolution is much larger than the ω natural width, we fit the $\pi^+\pi^-\pi^0$ distribution to a Gaussian (the mean, width, and area are fit parameters) plus a polynomial background. A clear ω signal is observed [Fig. 10(A)] with a mass of 783 ± 2 MeV. By plotting the $\pi^+\pi^-\pi^0$ mass in bins of $|t-t_{min}|$, we observe a forward diffractive peak [Fig. 11(A)].

Similarly, we define the two tracks not associated with the K_S^0 as charged kaons, plot the K^+K^- invariant mass, and fit the distribution to a resoluted Breit-Wigner (the mean, measured width and area are fit parameters, the natural width of the ϕ is fixed) plus a polynomial background. Without Cherenkov identification, a clear ϕ signal is found [Fig. 10(B)] with a mass of 1.020 ± 2 MeV. Again we bin the K^+K^- invariant mass in bins of $|t-t_{min}|$ and observe the diffractive forward peak [Fig. 11(B)].

The $K_S^0\pi^+\pi^-K_S^0\omega$ and $K_S^0\phi\,|t-t_{min}|$ distributions were fit to the sum of two exponentials in $|t-t_{min}|$. The curves from these exponential fits have been superimposed in Figs. 9, 10, and 11. The results are summarized in Table I. All three reactions are consistent with production from a carbon nucleus plus an incoherent and noncoherent background.

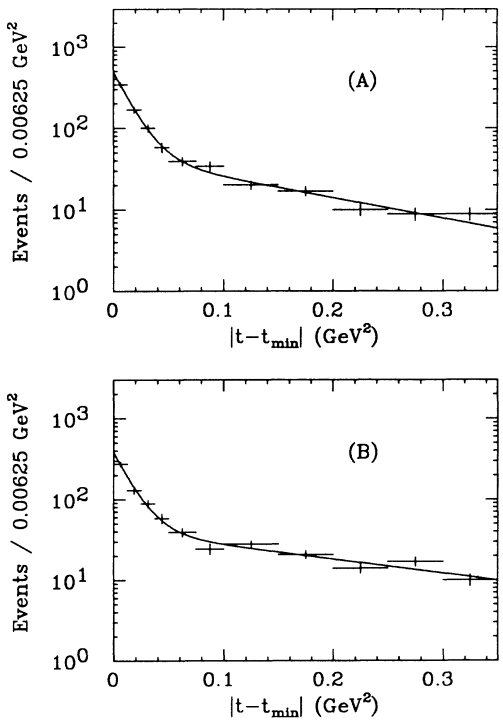

FIG. 11. $|t-t_{min}|$ for (A) $K_S^0\omega$ and (B) $K_S^0\phi$ events satisfying diffractive cuts. The solid lines represent a fit of the distributions to a sum of two exponentials.

TABLE I. Diffractive slope for K_L^0 diffraction dissociation final states. This value is the b parameter in the expression $d\sigma/d\,|t|\propto e^{bt}$ in the diffractive region.

Final state	Diffractive $\lvert t-t_{\min}\rvert$ slope (GeV^{-2})
$K_S^0\pi^+\pi^-$	66±2
$K_S^0\omega$	64±7
$K_S^0\phi$	63±10

B. Cross sections versus $\sqrt{s}$

Using the diffractive cuts outlined above, including the $|t-t_{\min}|<0.05$ $(\mathrm{GeV}/c)^2$ requirement, we plot the cross section/per target nucleus as a function of laboratory energy (Fig. 12). The background for the ω and the ϕ in the $K_S^0\omega$ and $K_S^0\phi$ cross section is statistically subtracted using the fitting procedure described in Sec. V A. All three distributions are consistent with having a cross section which is independent of laboratory energy although the $K_S^0\pi^+\pi^-$ exhibits a rise above 150 GeV. This increase may be due to a lack of understanding of the extreme upper limit of the K_L^0 spectrum or perhaps contamination from high-energy neutrons produced by charge exchange in the primary target.

C. Mass distributions and their energy dependence

Figures 13(A)–13(F) show the invariant-mass distributions for $K_S^0\pi^+\pi^-$, $K_S^0\omega$, and $K_S^0\phi$, corrected for accep-

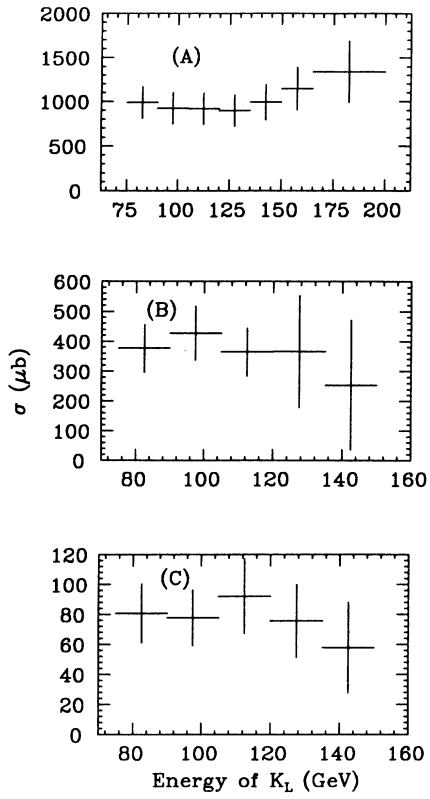

FIG. 12. Cross section/nucleus for (A) $K_S^0\pi^+\pi^-$, (B) $K_S^0\omega$, and (C) $K_S^0\phi$ diffractive final states.

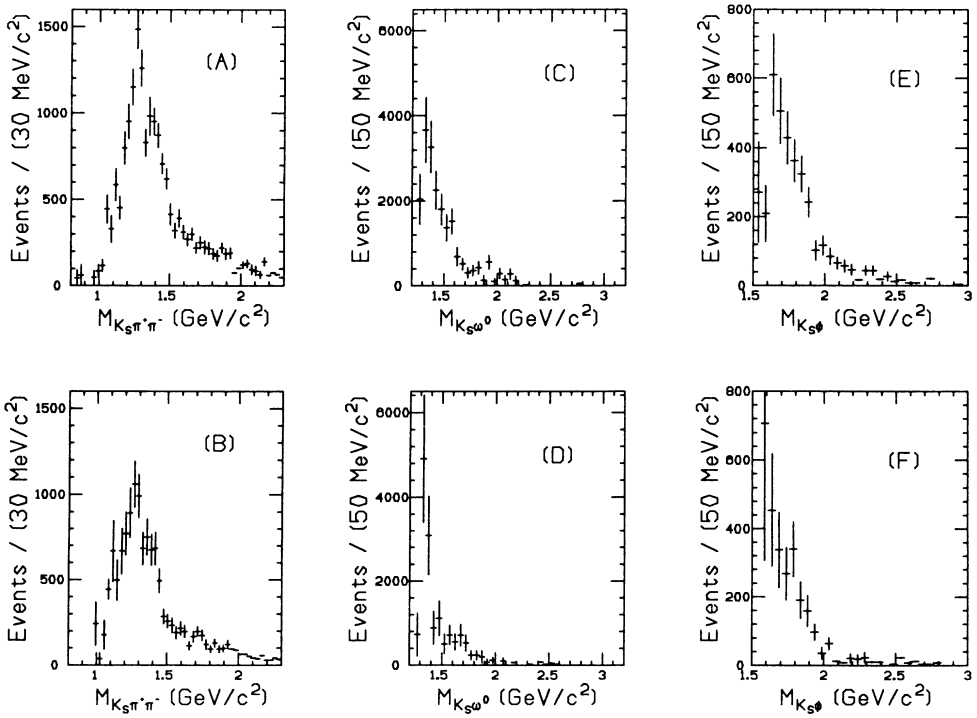

FIG. 13. Mass distribution of $K_S^0\pi^+\pi^-$, $K_S^0\omega$, and $K_S^0\phi$ in low- and high-energy bins. The energy range for (A) $K_S^0\pi^+\pi^-$, (C) $K_S^0\omega$, and (E) $K_S^0\phi$ is from 75 to 112 GeV. The energy range for (B) $K_S^0\pi^+\pi^-$, (D) $K_S^0\omega$, and (F) $K_S^0\phi$ is from 112 to 150 GeV.

tance, which satisfy our diffractive criterion 1–4, in bins of high energy and low energy. For these plots, the ω and the ϕ events contain the appropriate invariant submass to within 25 and 8 MeV/c^2 of their respective published values (783 and 1020 MeV/c^2). This definition of the ω and ϕ introduces a signal to noise of about 1.

Each distribution has the characteristic 400–500 MeV/c^2 mass threshold enhancement associated with a diffractive-inelastic production. Note that the $K_S^0\omega$ and the $K_S^0\pi^+\pi^-$ have been identified in charged-kaon interactions as the "K_1 meson," members of the 1^{++} and 1^{+-} SU(3) nonets.[2] Although a partial-wave analysis is not practical because of the lack of statistics and the large background for the $K_S^0\omega$ and $K_S^0\phi$, it is interesting to note that the shape of the mass distributions do not change appreciably as the laboratory energy changes from 75 to 150 GeV in any of these distributions. We also find no obvious enhancement for diffractively produced $K_2(1780)$ meson$\rightarrow K_S^0\omega$, $K_S^0\pi^+\pi^-$ production in our data [Figs. 13(A)–13(D)]. Despite this lack of a positive signal, the $K_S^0\omega$ and $K_S^0\pi^+\pi^-$ mass spectra in our data are in statistical agreement with previously reported spectra[10] which observe clearer evidence for the $K_2(1780)$ meson in the scattering of charged kaons on hydrogen at 14 and 32 GeV/c.

D. Resonance analysis of the $K_S^0\pi^+\pi^-$ final state

Figure 14 shows the $K_S^0\pi^+$, $K_S^0\pi^-$, and $\pi^+\pi^-$ submass for the $K_S^0\pi^+\pi^-$ system. The charged K^* and the ρ are clearly visible. For comparison to the quasi-two-body states near mass threshold in the next section, we would like to measure the production of $K^{*\pm}\pi^{\mp}$ and $K_S^0\rho$ from diffractively produced $K_S^0\pi^+\pi^-$ as a function of the $K_S^0\pi^+\pi^-$ mass.

Like the ω and ϕ from $K_S^0\omega$ and $K_S^0\phi$, the ρ and K^* signal-to-noise ratio is of order unity and so the background must be subtracted statistically. In order to determine the amount of $K_S^0\rho$ and $K^{*\pm}\pi^{\mp}$ in the diffractively produced $K_S^0\pi^+\pi^-$, we fit the K^* and ρ to Breit-Wigner distributions. This is because our resolution for reconstructing these two resonances is much smaller than the natural width of each resonance. However, the situation is complicated by the fact that the Breit-Wigner distribution of the ρ and K^* is distorted because the mass of the $K_S^0\pi^+\pi^-$ system tends to cluster toward the mass threshold. This is particularly true for the ρ whose 150-MeV/c^2 natural width is comparable to the observed 400-MeV/c^2 threshold enhancement. In order to include these phase-space distortion effects, we model resonance production within a small $K_S^0\pi^+\pi^-$ mass interval by generating uniform $K_S^0\pi^+\pi^-$ phase space weighted by the appropriate Breit-Wigner squared matrix element. This produces a Monte Carlo K^* and ρ subresonance with the appropriate shape for that $K_S^0\pi^+\pi^-$ mass interval. Since the K^* distribution is much less distorted than the ρ, we start by fitting the $K_S^0\pi$ mass distribution to a linear combination of the Monte Carlo–deduced K^* distribution plus the expected background from $K_S^0\rho$, $K^{*\pm}\pi^{\mp}$ (wrong combination) and

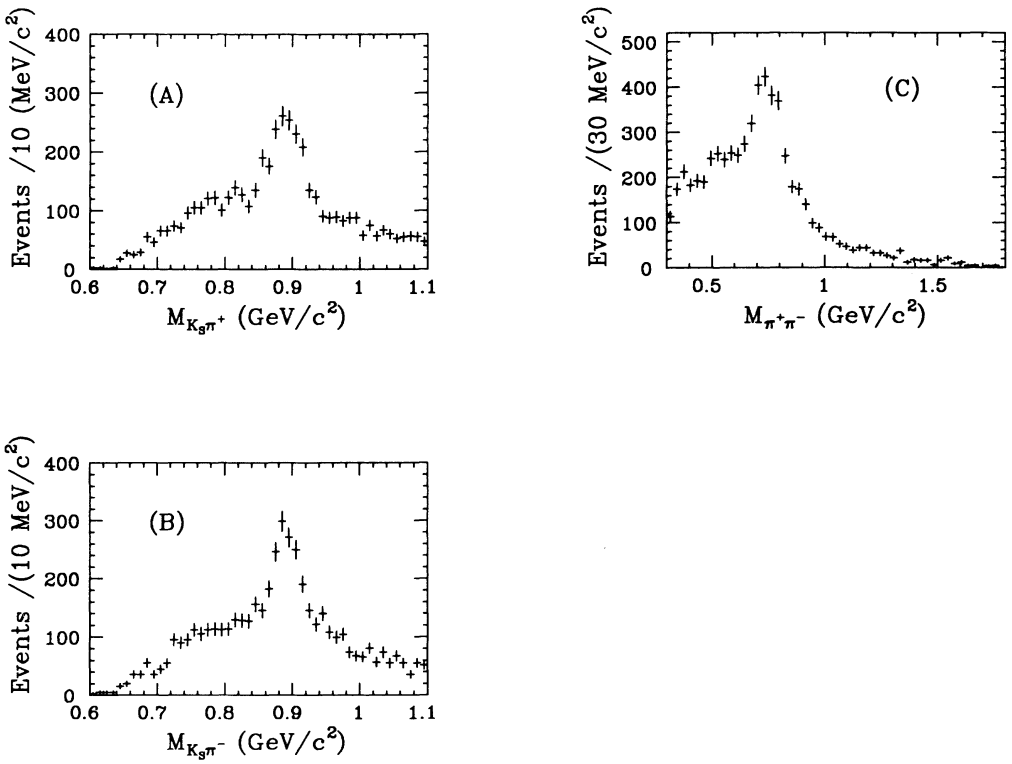

FIG. 14. Subresonance for $K_S^0\pi^+\pi^-$: (A) $K_S^0\pi^+$, (B) $K_S^0\pi^-$, and (C) $\pi^+\pi^-$.

$K_S^0\pi^+\pi^-$ phase space. We also allow for a polynomial background in analogy to the fits to the ω and ϕ described in Sec. V A in order to model other backgrounds, i.e., broad resonances such as the $f_0(1300)$ and the $K_0^*(1350)$. The same procedure applies to the $K_S^0\rho$ distribution except that the $\pi^+\pi^-$ background from $K^{*\pm}\pi^{\mp}$ events, determined from the $K^{*\pm}\pi^{\mp}$ fit is used as a fixed input parameter.

E. Comparison of quasi-two-body cross sections in the threshold region

We define the threshold mass region for $K^{*\pm}\pi^{\mp}$, $K_S^0\rho$, $K_S^0\omega$, and $K_S^0\phi$, by a method similar to that used in Ref. 10. These quasi-two-body final states are all of the form $S+R$ where S is a stable particle and R is a resonance with a non-negligible width Γ_R. Let M_S be the mass of the stable particle and M_R be the "centroid" mass of the resonance. Letting M_F be the mass of the $K_S^0\pi^+\pi^-$ or $K_S^0\pi^+\pi^-\pi^0$ final state, we then define the threshold mass region by the relation

$$M_S+M_R-\frac{\Gamma_R}{2}<M_F<M_S+M_R+500\ \text{MeV}/c^2\ .$$

The 500-MeV/c^2 represents the approximate width of the observed mass threshold enhancements in these four final states. The $\Gamma_R/2$ is included in the lower limit to accommodate the width of the resonance.

For comparison of the $K^{*\pm}\pi^{\mp}$, $K_S^0\rho$, $K_S^0\omega$, and $K_S^0\phi$, we restrict ourselves to laboratory energies between 75 and 125 GeV. Because of acceptance and the falling K_L^0 spectrum, most of the data lies in this energy region.

Using our standard diffractive cuts and the above threshold mass criterion, we can compute the cross section/nucleus for coherent production of $K_S^0\omega$, $K_S^0\phi$, $K_S^0\rho$, and $K^{*\pm}\pi^{\mp}$. The results are shown in Table II and Fig. 15.

This data can be compared to Givenaud *et al.*, who studied the diffraction dissociation of charged kaons on a proton target at beam momenta of 32 and 14 GeV/c. Givenaud *et al.* showed that final states which involve the creation of $s\bar{s}$ pairs appear to be suppressed relative to final states involving $u\bar{u}$ pairs by a factor of 3–4 (after compensating for the fall off of production cross section with increasing threshold mass). The ratio

$$\frac{\sigma(K\omega)+\sigma(K\rho)}{2\sigma(K\phi)}$$

was measured to be 3.9±0.6 in the Givenaud paper which is indicative of the level of strange-quark suppression. This ratio was measured to be 5±1 in our data which compares well with the Givenaud measurements. The ratio reflects strange-quark suppression as well as threshold mass effects. Although we do not have sufficient data to correct our ratio for the mass threshold suppression, it is of interest to note that the ratio obtained in our experiment, taken with a 75–125-GeV K_L beam on a nuclear target, agrees with data taken with a low energy $K^{\pm}$ beam on a hydrogen target.

TABLE II. Cross section per nucleon obtained for quasi-two-body K_L^0 diffraction dissociation final states in the threshold mass region (defined in text). These cross sections are for laboratory energies between 75 and 125 GeV.

Decay mode	σ/nucleus (μb)
$K^*(890)^{\pm}\pi^{\mp}$	539±90
$K_S\rho$	258±63
$K_S\omega$	364±64
$K_S\phi$	62±11

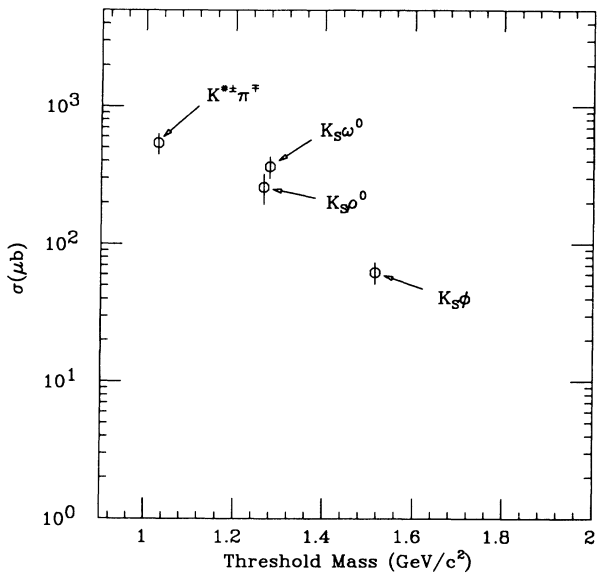

FIG. 15. Total cross section versus threshold mass for two-body diffraction dissociation final states.

VI. CONCLUSION

Plots of the reaction $K_L^0+C\rightarrow C+X$ where X has the form $K_S^0\pi^+\pi^-$, $K_S^0\phi$, or $K_S^0\omega$, exhibit a $|t-t_{\min}|$ distribution with a steep forward peak indicative of a coherent K_L^0-carbon scattering. Coherent scattering allows us to tag the exclusive production of two- and three-body diffraction dissociation final states.

Demanding that the events lie in the forward $|t-t_{\min}|$ peak, we observe mass threshold enhancements in $K_S^0\phi$, $K_S^0\omega$, and in $K_S^0\pi^+\pi^-$. Analysis of the $K_S^0\pi^+\pi^-$ final state indicates a large level K^* and ρ subresonance production. We find that the cross section for these final states is essentially independent of energy above 75 GeV, but not inconsistent with a slight increase or decrease with laboratory energy. Thus, these states have the qualitative features of a diffractive inelastic resonance mechanism.

We compute the cross section for diffractive mass threshold production of $K^{*\pm}\pi^{\mp}$, $K_S^0\rho$, $K_S^0\omega$, and $K_S^0\phi$. The ratios of threshold production of these four final

states compare well with earlier published results on the diffraction dissociation of charged kaons on hydrogen at 14 and 32 GeV/c. These earlier results indicated that production cross sections decrease with increasing threshold mass and that processes which involve the creation of strange quarks are suppressed by a factor of 3–4 relative to processes which do not require the production of strange quarks.

ACKNOWLEDGMENTS

We wish to acknowledge the professional staff and facilities of the Fermi National Accelerator Laboratory, the University of Illinois, and Columbia University. This work was supported through grants from the U.S. Department of Energy and the National Science Foundation.

---

[a]Present address: Fermi National Accelerator Laboratory, Batavia, IL 60510.
[b]Present address: University of Florida, Gainesville, FL 32601.
[c]Present address: Argonne National Laboratory, Argonne, IL 60439.
[d]Present address: Stanford Linear Accelerator Center, Stanford, CA 94305.
[e]Present address: Notre Dame University, South Bend, IN 46556.
[f]Present address: AT&T Bell Laboratories, Holmdel, NJ 07974.
[g]Present address: University of Colorado, Boulder, CO 80309.
[h]Present address: Brookhaven National Laboratory, Upton, NY 11973.
[i]Present address: University of Massachusetts, Amherst, MA 01003.
[j]Present address: California Institute of Technology, Pasadena, CA 91125.

[1]M. J. Lamm, Ph.D. thesis, University of Illinois, 1983.
[2]C. Daum *et al.*, Nucl. Phys. **B187**, 1 (1981).
[3]G. W. Brandenberg *et al.*, Phys. Rev. Lett. **36**, 703 (1976); **36**, 706 (1976).
[4]G. W. Brandenberg *et al.*, Nucl. Phys. **B45**, 397 (1972).
[5]T. C. Bacon *et al.*, Nucl. Phys. **B162**, 189 (1980).
[6]M. C. Goodman *et al.*, Phys. Rev. D **22**, 537 (1980).
[7]R. T. Edwards *et al.*, Phys. Rev. D **18**, 76 (1978).
[8]J. Greenhalgh (private communication).
[9]R. Egloff, Ph.D. thesis, University of Toronto, 1978.
[10]A. Givenaud *et al.*, Z. Phys. C **8**, 291 (1981).